Acta Materialia 304 (2026) 121798

Contents lists available at ScienceDirect

Acta Materialia

journal homepage: www.elsevier.com/locate/actamat

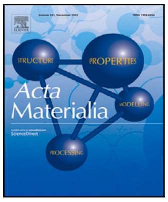

Full length article

Microstructure and orientation effects on microcompression-induced plasticity in nanoporous gold

Tim Fischer [a],*, Norbert Huber [a,b]

[a] Institute of Materials Physics and Technology, Hamburg University of Technology, Eißendorfer Straße 42, Hamburg, D-21073, Germany
[b] Bundesanstalt für Materialforschung und -prüfung (BAM), Unter den Eichen 87, Berlin, D-12205, Germany

ARTICLE INFO

Keywords:
Nanoporous gold
Microcompression
Plasticity
Size effect
Micromechanics

ABSTRACT

Understanding the plastic deformation of nanoporous metals requires a detailed examination of their small-scale microstructural features. In this work, we present a computational study of micropillar compression in single crystal nanoporous gold (NPG) using crystal plasticity. This approach enables a systematic investigation of three key microstructural effects, including ligament size ($50 \leq l \leq 400$ nm), solid fraction ($0.2 \leq \varphi \leq 0.3$), and initial crystal orientation ([001] and [$\bar{1}$11]), on the plastic response far beyond yielding. After validation against experimental data, the study reveals that, in line with the 'smaller is stronger' trend, besides the yield strength, the strain hardening rate also increases as ligament size decreases. Moreover, the strain hardening rate follows a power-law scaling with solid fraction, similar to the yield strength. The analysis of two distinct crystal orientations presents findings contrasting with previous assumptions. While the yielding onset remains orientation-independent, as expected, an increase in the strain hardening rate emerges for the harder [$\bar{1}$11] orientation with continued compression. An effect that becomes more pronounced with increasing solid fraction and decreasing ligament size. Under these conditions, harder orientations also amplify local stress heterogeneity. Notably, the stress distribution in NPG is nearly twice as wide as that observed in the single crystal bulk material ($\varphi = 1.0$). Compared to the crystal plasticity approach, traditional isotropic plasticity predicts more uniform local stress fields.

1. Introduction

Nanoporous metals, particularly nanoporous gold (NPG), feature a highly interconnected network of nanoscale ligaments, exhibiting mechanical properties that differ significantly from their bulk counterparts. These materials are especially attractive due to their high ductility, tunable mechanical properties, and functional versatility [1–6]. The mechanical response is governed by a complex interplay of nanoscale plasticity, surface effects, and deformation mechanisms at the ligament scale. Gaining a comprehensive understanding of these interactions is crucial for optimizing NPG in applications such as energy storage, catalysis, and biomedical devices, where both structural integrity and functional performance are essential.

The mechanical behavior of NPG is predominately controlled by microstructural factors such as ligament size, solid fraction, shape, and distribution, which dictate its yielding and failure mechanisms [7–12]. Unlike conventional metals, where strength arises from numerous bulk dislocation interactions, NPG exhibits size-dependent strengthening due to few dislocations confined within its nanoscale ligaments, often following a Hall–Petch-like scaling [13–16]. The nanoscale ligament network imposes severe geometric constraints on dislocation motion, introducing strain gradients that likely activate geometrically necessary dislocations (GNDs), thereby enhancing strength [17–19]. In addition, high ligament curvature can generate stress gradients affecting dislocation nucleation and glide, while the large surface-to-volume ratio limits dislocation storage but promotes surface diffusion and capillary effects, leading to time-dependent deformation phenomena [20–25]. Also, ligament junctions typically serve as pinning points, restricting dislocation motion and inducing localized hardening, though they can also trigger strain localization and failure [20]. Pre-existing defects, such as vacancies and twin boundaries, further impede dislocation mobility [26]. Beyond these intrinsic effects, crystallographic orientation may also influence the material's mechanical properties due to the anisotropic nature of the crystal lattice. While strength and deformation behavior generally vary with stress direction in single crystal bulk, recent studies suggest that the onset of plastic flow in NPG remains largely insensitive to orientation, yet its role at larger deformations remains an open question [21,27–29].

---

* Corresponding author.
E-mail address: tim.fischer@tuhh.de (T. Fischer).

https://doi.org/10.1016/j.actamat.2025.121798
Received 14 July 2025; Received in revised form 24 November 2025; Accepted 1 December 2025

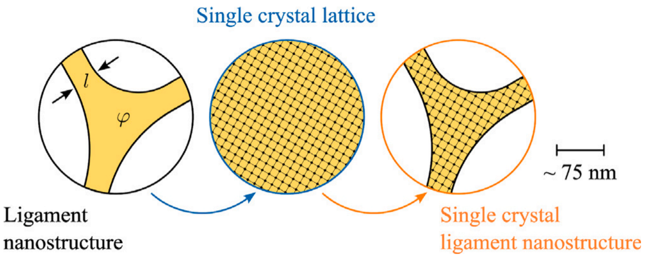

Fig. 1. Schematic of the nanoscale ligament network. The NPG microstructure is characterized by ligament size l and solid fraction φ. Plastic deformation is modeled using a crystal plasticity formulation, accounting for single crystal behavior and crystallographic orientation.

To characterize the mechanical behavior of NPG and its fully dense gold counterparts at the microscale, advanced micromechanical testing methods such as micropillar compression and microtensile testing are commonly employed [26,29–40]. These techniques enable precise measurements of key mechanical properties, including yield strength, strain hardening, and failure mechanisms, while providing valuable insights into the impact of ligament architecture and size effects on local deformation mechanisms. To facilitate result interpretation and mechanistic insights, these intricate and time-consuming tests are often supplemented with finite element method (FEM) simulations [17,41–52]. However, computational plasticity studies have so far been limited to fully dense bulk variants. Apart from macroscale FEM studies relying on representative volume elements (RVEs) [53–56,56–61], FEM-based simulations explicitly accounting for nanoporous metals remain unexplored. This work aims to bridge this gap by presenting single crystal microcompression simulations of NPG, incorporating crystal plasticity. The computational study systematically explores the effects of three key intrinsic microstructural factors on plastic deformation within the following bounds up to large strains:

1. Ligament size ($50 \leq l \leq 400$ nm)
2. Solid fraction ($0.2 \leq \varphi \leq 0.3$)
3. Initial crystal orientation ([001] and [$\bar{1}$11])

In this work, Section 2 presents an overview of the material and experimental background that motivate our modeling efforts. Section 3 details the simulation methodology, which models the ligament network as a single crystal nanostructure (Fig. 1). After model validation against most recent experimental data, Section 4 examines the impact of the three microstructural features on the plastic response, with concluding remarks provided in Section 5.

2. Materials and experimental methods

To establish a meaningful micromechanical model, key parameters defining experimental samples from literature are summarized below. NPG as modeled here is typically fabricated via dealloying, where a less noble element is selectively removed from an alloy, leaving a bicontinuous gold network [5,62]. The most common precursor alloy is Ag-Au, where silver is selectively dissolved in an acid or electrochemical bath. The resulting structure consists of a network of nanoscale ligaments and pores, see Fig. 2(a), whose morphology can be tailored through processing conditions. The solid fraction, representing the volume fraction of gold remaining after dealloying, typically ranges between 0.2 and 0.4. Lower solid fractions ($\varphi \approx 0.2$) result from more extensive dealloying, producing a more open structure, whereas higher solid fractions ($\varphi \approx 0.4$) occur with shorter dealloying times or milder conditions, preserving more gold content. In its as-dealloyed state, the ligament size typically falls between 10 and 50 nm. However, post-processing treatments such as thermal annealing can induce coarsening, increasing ligament sizes to 50–500 nm through surface diffusion. Additionally, electrochemical treatments allow for precise control over ligament size by adjusting applied potential or electrolyte composition.

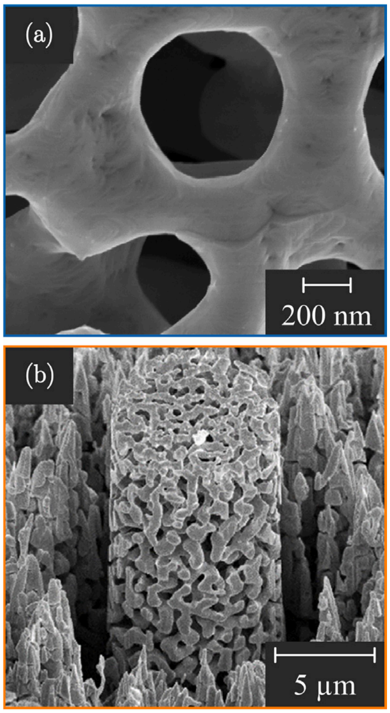

Fig. 2. Scanning electron microscope (SEM) images of NPG showing the interconnected network of nanoscale ligaments (a) and corresponding micropillar (b). The ligament size is $l = 330$ nm, and the solid fraction is $\varphi = 0.2$.
Source: Adapted from [20], under CC BY license.

The single crystal microcompression method involves fabricating micropillars with well-defined dimensions and crystal orientations, see Fig. 2(b), followed by uniaxial compression using a nanoindenter equipped with a flat punch. To shape individual micropillars with controlled aspect ratios, typically ranging from 2:1 to 4:1 (height-to-diameter), focused ion beam (FIB) milling is employed [26,29–32,36,40]. While FIB milling allows for precise control over pillar dimensions, it often introduces a slight taper, making the pillars not perfectly straight [50–52]. Additionally, a small curvature at the pillar base is common due to the ion milling process, potentially influencing stress distributions and deformation behavior [41,50–52,63]. Crystal orientations are often unspecified in NPG microcompression studies, as the material is generally assumed to exhibit orientation-independent behavior [27,29]. During testing, the micropillars are compressed at controlled displacement rates, typically ranging from 10^{-4} to 10^{-2} 1/s, ensuring quasi-static loading conditions. Stress–strain curves are constructed by measuring the applied load or displacement during compression. The engineering stress σ is determined by dividing the applied force by the initial cross-sectional area of the micropillar, while the engineering strain ε is obtained from the displacement normalized by the initial pillar height.

3. Simulation methods

3.1. Constitutive model

The crystal plasticity finite element method (CPFEM), in its phenomenological formulation proposed by Huang [64], is employed to systematically investigate the intrinsic effects on the microcompression response. This approach accounts for finite strain and rotation effects. To distinguish between elastic $\mathbf{F}_\mathrm{e}$ and plastic $\mathbf{F}_\mathrm{p}$ deformation components, the deformation gradient is multiplicatively decomposed as $\mathbf{F} = \mathbf{F}_\mathrm{e}\mathbf{F}_\mathrm{p}$. The material's actual stress state is then determined using the generalized Hooke's law, expressed as $\mathbf{S} = \mathbb{C} : \mathbf{E}$. This formulation relates the elastic Green–Lagrange strain $\mathbf{E}$ to the second Piola–Kirchhoff stress $\mathbf{S}$ through the elastic stiffness tensor $\mathbb{C}$. Given the identity tensor $\mathbf{I}$, the Green–Lagrange strain is computed as $\mathbf{E} = 1/2\left(\mathbf{F}_\mathrm{e}^\mathrm{T}\mathbf{F}_\mathrm{e} - \mathbf{I}\right)$. The elastic stiffness tensor $\mathbb{C}$ reflects the symmetry of the underlying crystal lattice, reducing the number of independent elastic constants to three: C_{11}, C_{12}, and C_{44}. The plastic contribution to deformation, driven by dislocation slip, is characterized by the plastic velocity gradient $\mathbf{L}_\mathrm{p}$. Here, crystal plasticity manifests through the accumulation of slip on multiple slip systems. The plastic velocity gradient is expressed as the sum of the slip rates $\dot{\gamma}^\alpha$ over all N_s slip systems

$$\mathbf{L}_\mathrm{p} = \dot{\mathbf{F}}_\mathrm{p}\mathbf{F}_\mathrm{p}^{-1} = \sum_{\alpha=1}^{N_\mathrm{s}} \dot{\gamma}^\alpha\, \mathbf{m}^\alpha \otimes \mathbf{n}^\alpha\,, \tag{1}$$

where $\mathbf{m}^\alpha$ represents the slip direction and $\mathbf{n}^\alpha$ denotes the slip plane normal for a given slip system α [65]. To qualify the material hardening, a phenomenological description is deployed. On each slip system, the shear rate progresses according to the power law proposed by [66–68]

$$\dot{\gamma}^\alpha = \dot{\gamma}_0 \left|\frac{\tau^\alpha}{g^\alpha}\right|^{\frac{1}{m}} \operatorname{sgn}(\tau^\alpha)\,, \tag{2}$$

where $\dot{\gamma}_0$ is the reference shear rate and τ^α the resolved shear stress opposed to the current strength or critical resolved shear stress g^α (CRSS). Strain rate sensitivity is reflected by the material parameter m. How the slip system β affects the hardening behavior of system α is mirrored in the CRSS evolution by

$$\dot{g}^\alpha = \sum_{\beta=1}^{N_\mathrm{s}} h_{\alpha\beta}\, \dot{\gamma}^\beta\,, \tag{3}$$

where $h_{\alpha\beta} = q\, h(\gamma)$ is the interaction hardening matrix with the functional form of

$$h(\gamma) = h_0 \operatorname{sech}^2\left|\frac{h_0\gamma}{\tau_\mathrm{s} - \tau_0}\right|\,, \tag{4}$$

determining the micromechanical interaction between the different systems through the constant q. This constant sets the level of latent hardening as compared to self hardening. For all slip systems, the initial hardening modulus h_0, saturation strength τ_s, and initial strength τ_0 are identical. The initial strength or CRSS (in MPa) is scaled as a function of the NPG ligament size l (in nm) following a Hall–Petch type relationship [69,70]

$$\tau_0 = 5939 \cdot l^{-1.22}\,, \tag{5}$$

where the pre-factor represents the efficiency of dislocation motion impediment. This relationship, illustrated in Fig. 3, is obtained by fitting experimental yield strength data from single crystal microcompression tests across various ligament sizes at $\varphi = 0.3$ [29]. Notably, it aligns well with other microcompression data for varying solid fractions φ and pillar height-to-diameter ratios h/d [20,27,32]. The equivalence between measured yield strength σ_y and initial CRSS in the model ($\sigma_\mathrm{y} \approx \tau_0$) suggests that plasticity in NPG initiates at the ligament scale rather than being governed by bulk constraints. Given that the theoretical shear strength of ligaments exceeds 1 GPa [30,40], τ_0 should therefore be interpreted as an effective value. To further clarify, the size effect is introduced through the ligament size-dependent τ_0, which represents the collective response of interacting ligaments rather than the intrinsic strength of individual ones [71]. Similar CPFEM studies on NPG [27] have used plastic parameters derived from the flow behavior of polycrystalline gold [72], yielding comparable CRSS magnitudes. Alternatively, τ_0 could be calibrated using microcompression data from single crystal gold nanopillars with ligament-scale diameters [73], however, such data are limited to pillar diameters of a few hundred nanometers and are not available for the wide range of ligament sizes analyzed here. Moreover, assigning locally varying material properties poses additional challenges, especially for stochastic microstructures. The constitutive model is implemented in the commercial FEM software Abaqus using a material subroutine [64]. The elastic and crystal plasticity parameters for face-centered cubic (fcc) NPG are summarized in Table 1. The elastic constants C_{11}, C_{12}, and C_{44}, along with the reference shear rate $\dot{\gamma}_0$ and initial hardening modulus h_0, are adopted from [33]. For the strain rate sensitivity parameter m a typical value if 0.1 is used [64]. The ratio of latent to self-hardening moduli q is set to unity, implying no latent hardening [64]. Additionally, to account for size-dependent hardening effects, the ratio τ_s/τ_0 is fixed to a value of 4.0.

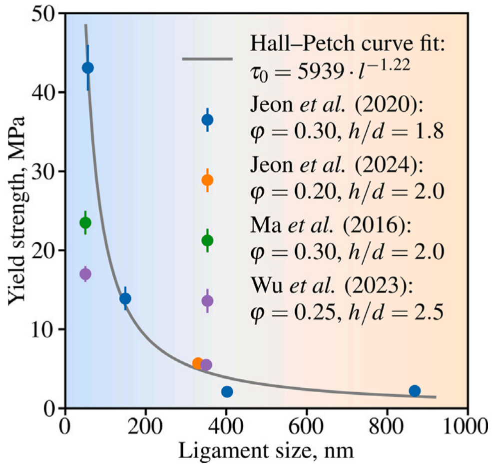

Fig. 3. Yield strength measured from single crystal microcompression experiments on NPG as a function of ligament size. In addition to ligament size, the solid fraction φ and the pillar height-to-diameter ratio h/d vary. The solid line represents a Hall–Petch type curve fit to the experimental data from [29].

Table 1
Elastic constants and crystal plasticity parameters of NPG [33,64]. Plastic deformation occurs on the 12 octahedral fcc slip systems $\{111\}\langle 110\rangle$.

Property	Value	Unit
C_{11}	186	GPa
C_{12}	157	GPa
C_{44}	42	GPa
$\dot{\gamma}_0$	0.001	1/s
m	0.1	–
h_0	2000	MPa
τ_0	Eq. (5)	MPa
τ_s	$4.0 \cdot \tau_0$	MPa
q	1.0	–

3.2. Microstructure model and boundary conditions

Fig. 4(c–f) presents the microstructure models for NPG microcompression at solid fractions φ of 0.2, 0.25, 0.3, and 1.0, along with their corresponding half-sections in (g–j). The latter solid fraction ($\varphi = 1.0$) represents the single crystal bulk material, resembling testing a single ligament. The porous microstructures are constructed based on an fcc-type diamond lattice arrangement [54], see Fig. 4(a), which provides a three-dimensional (3D), open-cell framework with fourfold coordinated nodes. To capture the characteristic morphology of NPG, the ligament junctions are modified to exhibit a smooth curvature approximately equal to the ligament diameter, resulting in a continuous transition

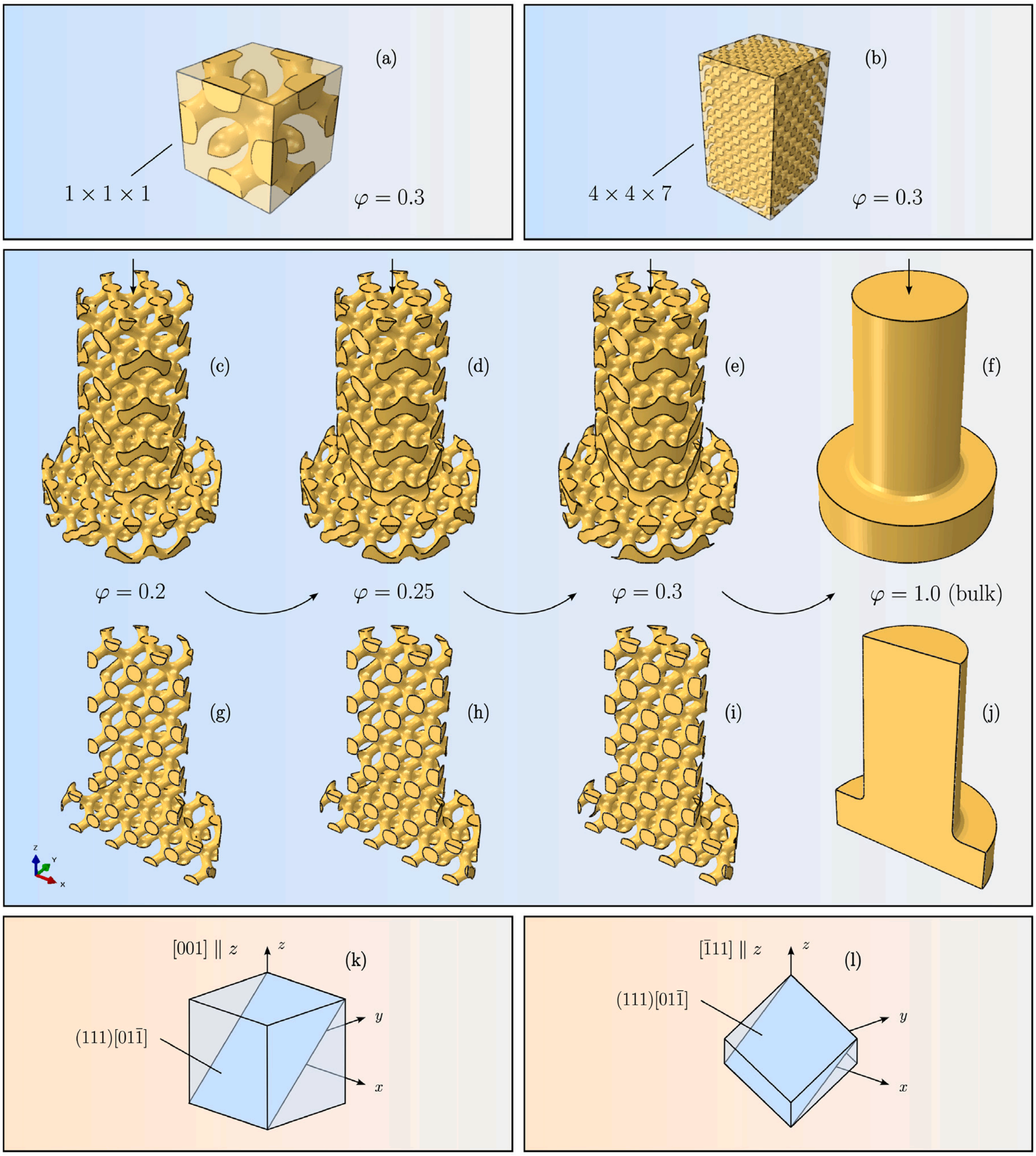

Fig. 4. Porous microstructure unit cell of NPG based on a diamond lattice with curvated ligament junctions (a), and its periodic extension (b). Micropillar compression models generated from the periodic structure for solid fractions φ of 0.2 (c), 0.25 (d), 0.3 (e), and 1.0 (f), with the latter constituting the single crystal bulk material. All pillars rest with a slight curvature on a substrate, and the pillar height-to-diameter ratio is 2.0. Additionally, the corresponding half-sections are shown (g–j). The initial crystal orientations [001] and [$\bar{1}$11] are visualized in (k, l), with the (111)[01$\bar{1}$] slip system explicitly illustrated.

between ligaments and nodes. The geometry of a single unit cell serves as the fundamental building block and is periodically duplicated along all spatial directions, see Fig. 4(b), to form the micropillar models. This periodic approach ensures topological uniformity and facilitates systematic variation of the solid fraction φ by scaling the ligament diameter while maintaining the overall pillar dimensions. The resulting structures provide a physically representative and numerically stable basis for FEM simulations of the deformation behavior. The pillars are assumed to be cylindrical with a slight taper angle of less than 1° and rest on a larger substrate with a diameter twice that of the pillar. A curvature at the pillar base, approximately 10 % of the pillar diameter, is also incorporated. The pillars presented in Fig. 4(c–f) have a height-to-diameter ratio of approximately 2:1, while the substrate's ratio is around 1:4. Both the pillars and the substrate share the same crystallographic orientation and constitutive material parameters. Compression is applied via a rigid surface positioned above the pillar, with a Coulomb friction coefficient of 0.1 between the two surfaces [41]. The mesh consists of up to two million tetrahedral elements (C3D4) with linear shape functions and full integration, depending on the solid fraction. Boundary conditions are defined by fully constraining the substrate's bottom nodes, while the rigid surface moves downward in a displacement-controlled mode, replicating typical experimental

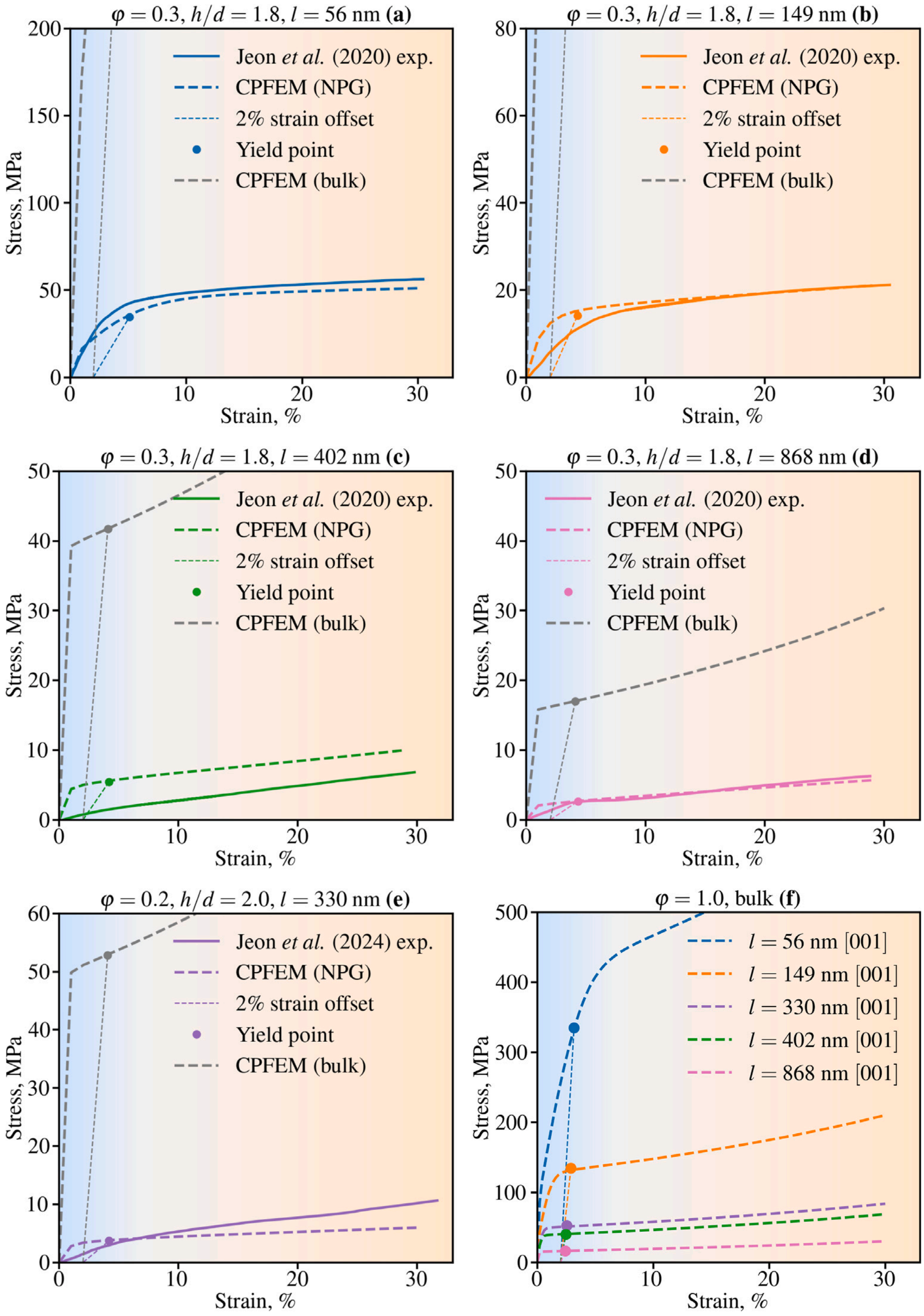

Fig. 5. Comparison of predicted and experimental stress–strain curves for different ligament sizes l, as well as solid fractions φ and height-to-diameter ratios h/d (a–e). Additionally, the single crystal bulk responses ($\varphi = 1.0$) for the individual ligament sizes are depicted (f). All predictions are performed on the initial [001] crystal orientation, with the yield point at 2 % strain offset marked.

conditions. The applied strain rate is 10^{-3} 1/s, and the NPG pillars are compressed up to a total strain ε of 30 %. The present study considers two initial crystal orientations: the kinematically softer [001] ([010] ∥ y) and the kinematically harder [$\bar{1}$11] ([110] ∥ y) orientation, both aligned with the compression z-direction, see Fig. 4 (k, l). The [001] orientation is highly stable under compression, whereas the [$\bar{1}$11] orientation is more prone to crystallographic reorientation under the given boundary conditions [27,41].

4. Results and discussion

4.1. Microstructure effect on stress–strain and scaling behavior

Fig. 5 compares the predicted and experimental stress–strain curves for different ligament sizes l, as well as solid fractions φ and height-to-diameter ratios h/d (a–e) [20,29]. Additionally, the predicted single crystal bulk responses ($\varphi = 1.0$) for the individual ligament sizes are depicted in Fig. 5(f). All calculations are performed on the initial [001] crystal orientation, with the yield point at 2 % strain offset marked. Flow stresses are compared at 2% strain to ensure analysis well within the plastic regime and consistency with experimental data, where the true elastic limit is often obscured and an apparent strength value at finite strain is typically reported [24,74]. Fig. 5(a–d) examine the effect of ligament size on the mechanical response while maintaining a solid fraction of $\varphi = 0.3$ and a height-to-diameter ratio of $h/d = 1.8$. As ligament size increases from 56 to 868 nm, the yield strength decreases significantly, perfectly aligning with the 'smaller is stronger' phenomenon [75,76], where the higher number of dislocation sources in larger ligaments raises the probability of early yielding [29]. This trend is reasonably well captured by the micromechanical model, closely matching the experimental data, with exception of $l = 402$ nm. In addition to the predicted reduction in yield strength, larger ligaments appear to trigger a more abrupt elastic–plastic transition. Early plasticity observed in the initial loading phase of all experimental curves is likely attributed to sample surface roughness or slight misalignment between the punch and the pillar [30]. Moreover, the inherent microstructural randomness, giving rise to a statistical distribution of local stress concentrations, can also contribute to this initial response. Consequently, minor deviations between simulations and experiments may arise from the simplified microstructural representation or limitations in capturing all underlying deformation mechanisms. Fig. 5(e) extends the analysis for model validation by considering a different solid fraction ($\varphi = 0.2$) with an aspect ratio of $h/d = 2.0$. Once again, showing reasonable agreement with the experimental data. The predicted yield strength here is slightly lower compared to predictions with $\varphi = 0.3$ at a similar ligament size of $l = 402$ nm, see Fig. 5(c). This is consistent with expectations, as a higher porosity leads to a reduction in load-bearing capacity and, consequently, lower strength. To further contextualize the mechanical response of NPG, Fig. 5(f) compares the predicted stress–strain behavior of bulk single crystal gold ($\varphi = 1.0$) with mechanical properties as determined for the different ligament sizes. As expected, the bulk material exhibits significantly higher yield strength, reaching up to ~ 500 MPa, and serves as a pore-free reference for the ligament size range explored in Fig. 5 (a–e). Generally, the simulations reproduce the well-known size-dependent strengthening trend, with smaller ligament sizes exhibiting higher yield strength and more pronounced hardening. While the model is based on a rather simplified geometric representation of the microstructure, it nonetheless captures the main experimental trends, supporting its utility as a framework for exploring the mechanical response of NPG.

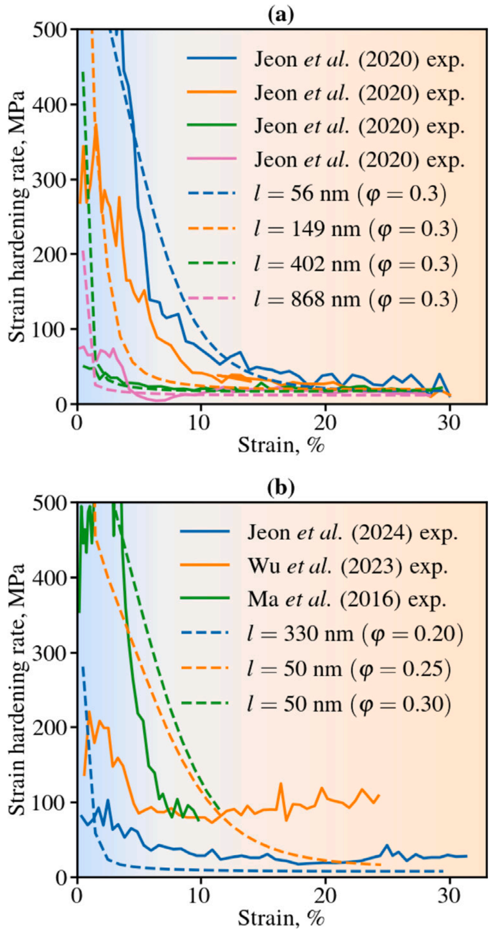

Fig. 6. Comparison of predicted and experimental strain hardening behavior for different ligament sizes l at a solid fraction of $\varphi = 0.3$ (a). For further validation, the predictions are compared with independent microcompression data at varying solid fractions (b). All predictions are performed on the initial [001] crystal orientation.

To more clearly assess the size-dependent strengthening, Fig. 6(a) shows the strain hardening rate $\theta = \mathrm{d}\sigma/\mathrm{d}\varepsilon$ as a function of ligament size at a fixed solid fraction of $\varphi = 0.3$, based on both experimental data [29] and corresponding simulations. For comprehensive validation, the predictions are compared in Fig. 6(b) with additional available microcompression data [20,27,32] obtained at varying solid fractions. Again, the predicted and experimental results reveal a pronounced size effect, with smaller ligament sizes exhibiting higher initial strain hardening rates. For example, in Fig. 6(a), the smallest ligament size ($l = 56$ nm) presents an initial hardening rate exceeding 400 MPa, while larger ligaments ($l = 402$ and 868 nm) display substantially lower rates. Although some studies report decreased strain hardening at smaller ligament sizes due to limited dislocation storage [29], our findings suggest enhanced hardening likely driven by dislocation accumulation and increased dislocation interactions [13,24]. While the CPFEM model does not explicitly resolve discrete dislocation processes, these interpretations are made in a qualitative sense, supported by atomistic and experimental observations in literature [13,24,29]. The simulated hardening trends are therefore viewed as phenomenological reflections of the collective ligament-scale plastic response, consistent with the mechanisms reported for NPG. Furthermore, as illustrated in Fig. 6(b), hardening also increases with higher solid fractions, as a denser ligament network enhances mechanical constraint and promotes more uniform distribution of plastic deformation. A power-law scaling of the strain hardening rate with solid fraction has been reported in [77]. Across all ligament sizes and solid fraction, the strain hardening rate decreases rapidly with increasing strain, stabilizing at lower values beyond approximately 10 % compression. This decline suggests a swift transition in the collective plastic response, from dislocation nucleation and interaction toward mechanisms dominated by dislocation annihilation or source exhaustion. The high fraction of free surfaces in NPG may further promote dislocation escape, limiting accumulation [29,78]. These interpretations are again made on a physically motivated basis, since the CPFEM framework operates at the continuum scale without resolving discrete dislocations, yet incorporates crystallographic slip and lattice anisotropy. Overall, the simulations capture the experimental trend, indicating that the model reasonably reflects key aspects of the strain hardening response. These findings highlight the critical role of ligament size in governing not only the yield strength but also the strain hardening behavior during microcompression of NPG.

Fig. 7 presents the ligament size-dependent scaling of the predicted normalized yield strength $\bar{\sigma}_\mathrm{y} = \sigma_\mathrm{y}/\sigma_\mathrm{y}^\mathrm{bulk}$ (a) and strain hardening rate $\bar{\theta} = \theta/\theta^\mathrm{bulk}$ (b). Yield strength is evaluated at a 2 % strain offset and strain hardening rate at 5 % compressive strain, both normalized by

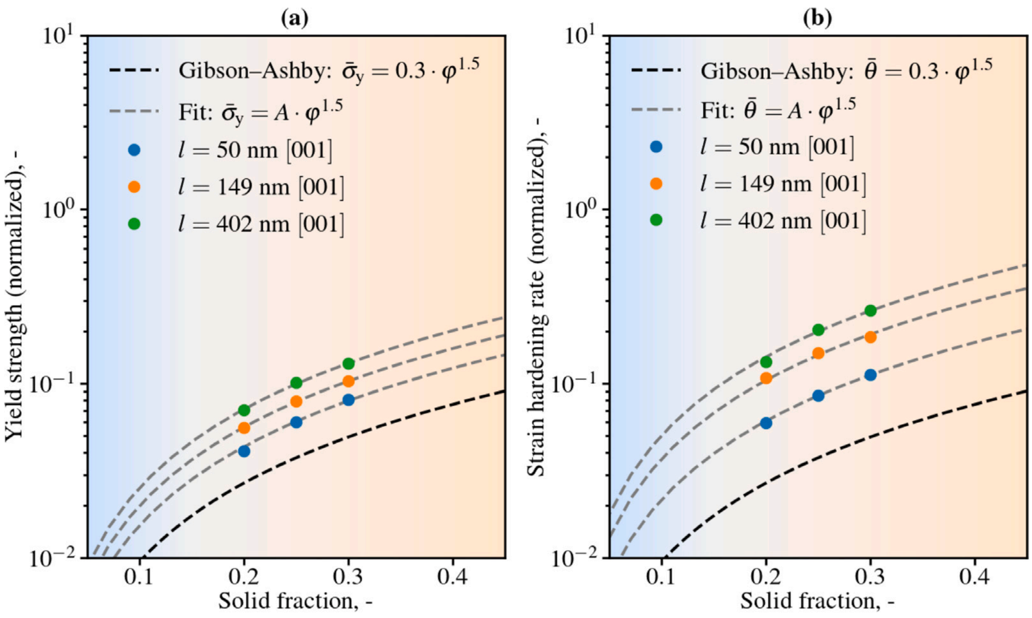

Fig. 7. Ligament size-dependent scaling of the predicted normalized yield strength (a) and strain hardening rate (b). Yield strength is determined at a 2 % strain offset and strain hardening rate at 5 % compressive strain, both normalized by the corresponding single crystal bulk values. All predictions assume an initial [001] crystal orientation. Dashed lines indicate the classical Gibson–Ashby scaling and a modified fit to the numerical data.

the corresponding single crystal bulk values, cf. Fig. 5(f). This normalization isolates the influence of ligament architecture (solid fraction) from the intrinsic material properties. It also enables comparison across ligament sizes and crystal orientations to assess whether NPG follows a consistent scaling law, revealing deformation mechanisms that are independent of absolute strength. All simulations assume the softer [001] crystal orientation. Three different solid fractions ($0.2 \leq \varphi \leq 0.3$) and ligament sizes ($50 \leq l \leq 400$ nm) are analyzed, highlighting the interplay between these parameters. The dashed lines represent the classical Gibson–Ashby scaling law $\bar{\sigma}_y \propto \varphi^{1.5}$ or $\bar{\theta} \propto \varphi^{1.5}$ [79], alongside modified power-law fits of the form $A \cdot \varphi^{1.5}$ applied to the numerical data. These fits account for differences in network geometry between the diamond unit cell and the original Gibson–Ashby architecture [54]. While the Gibson–Ashby relation cannot represent the loss of connectivity observed in stochastic networks at low solid fractions [60], it remains suitable for the periodic diamond architecture considered here. In this structure, uniform connectivity and regular load paths meet the assumptions of the scaling law and promote well-defined deformation modes. The same scaling exponent of 1.5 is applied to yield stress and hardening for consistency, as both plastic properties arise from similar ligament-level deformation mechanisms in the periodic architecture. While different exponents are in principle conceivable, using a shared exponent also provides a parsimonious description of the scaling behavior without overfitting the limited dataset. Despite the well-known trend of increasing strength with solid fraction, the data in Fig. 7(a) again reveal a pronounced ligament size effect, with larger ligaments exhibiting higher normalized yield strength. As a result, their mechanical response appears less sensitive to variations in solid fraction compared to smaller ligaments. In contrast to the classical Gibson–Ashby model, which assumes scale-independent plasticity, the results demonstrate that different ligament sizes systematically lead to distinct scaling behavior, hinting at a size-dependent correction to the strength scaling. Notably, the fitted curves for different ligament sizes appear largely offset versions of one another, suggesting that size effects remain qualitatively similar across varying solid fractions. Similar to the trend observed in Fig. 7(a), 7(b) demonstrates in this normalized presentation that the strain hardening rate exhibits a pronounced size effect, with larger ligaments appearing less sensitive to variations in solid fraction. The fitted curves for different ligament sizes display a comparable offset pattern as in the yield strength case. However, the scatter between the curves is more pronounced and uneven, suggesting that strain hardening is more strongly influenced here.

4.2. Orientation effect on stress–strain, scaling, and local stress behavior

The predicted stress–strain and strain-hardening rate curves in Fig. 8(a–c) and (d–f), respectively, illustrate the collective interplay of ligament size, solid fraction, and initial crystallographic orientation on the mechanical response of NPG. Across all solid fractions and ligament sizes, pillars oriented along the kinematically softer [001] direction exhibit a yield strength closely comparable to those oriented along the harder $[\bar{1}11]$ direction. This indicates that the yield strength remains largely independent of crystallographic orientation, aligning well with experimental observations [27,29]. However, beyond yielding, the flow stress and strain-hardening behavior exhibit a visible orientation dependence. Pillars oriented along $[\bar{1}11]$ consistently demonstrate a higher strain-hardening rate compared to their [001] counterparts. This suggests that plastic deformation in the $[\bar{1}11]$ direction involves more favorably oriented slip systems, increasing plastic slip activity and resistance to plastic flow. In contrast, pillars with a [001] orientation experience a more rapid decline in strain hardening, reflecting reduced slip activity and lower resistance to plastic flow. Limited to 10 % compression, this strain-hardening trend is also observed experimentally in [27]. The orientation dependence is more pronounced for smaller ligaments and higher solid fractions, see Fig. 8 (c, f). At the lowest solid fraction ($\varphi = 0.2$), the influence of orientation nearly diminished, although anisotropic differences in post-yield behavior remain observable. These results suggest that crystallographic orientation can play a role in shaping the strain-hardening response of NPG, even if its effect on the initial yield strength appears limited. Since NPG is able to undergo exceptionally large compression deformations, approaching 100 %, and reach nearly full density without failure, the observed

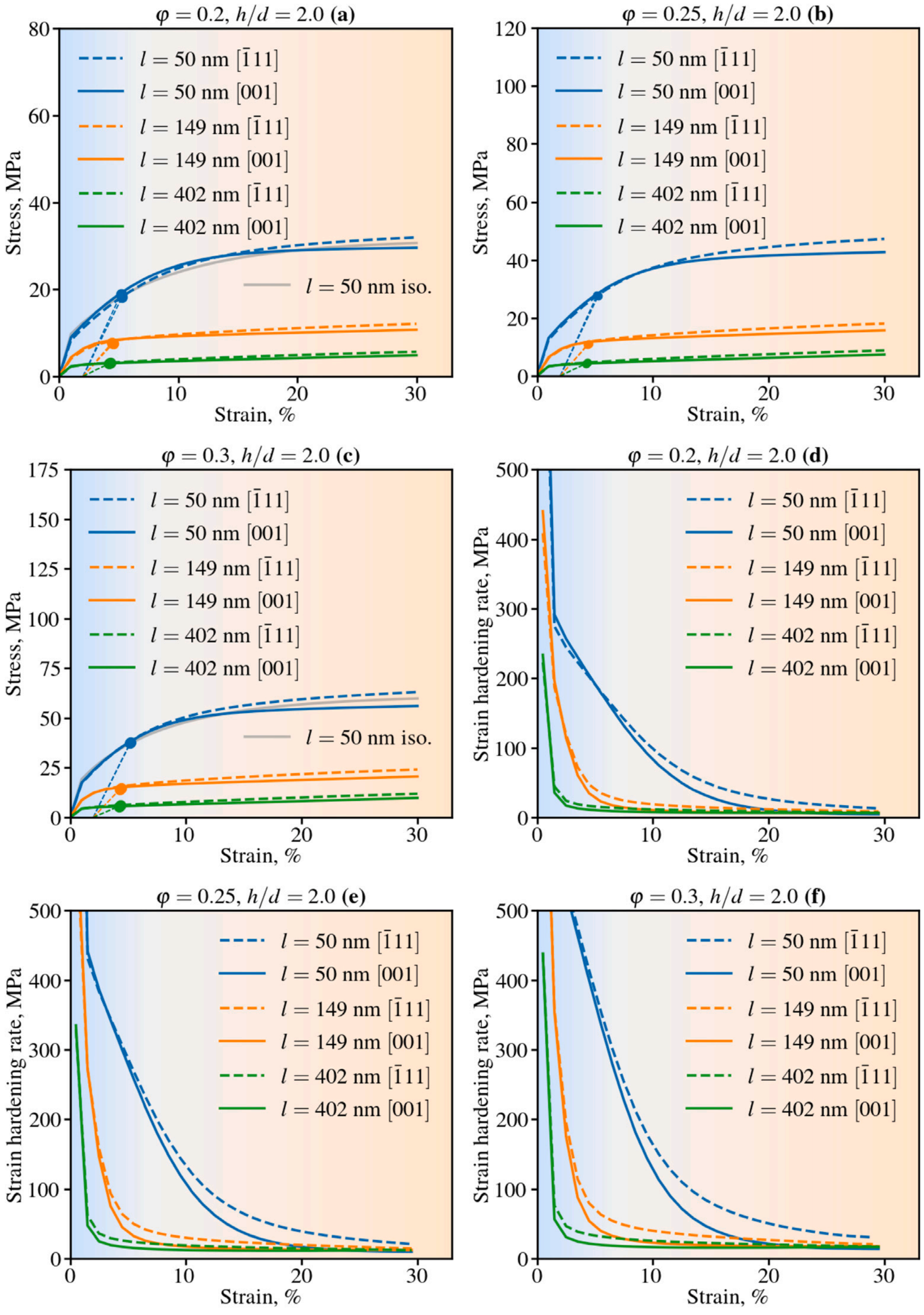

Fig. 8. Comparison of predicted stress–strain (a–c) and corresponding strain hardening curves (d–f) for the initial [001] and $[\bar{1}11]$ crystal orientations. The ligament sizes l are 50, 149, and 402 nm, with solid fractions φ of 0.2 (a, d), 0.25 (b, e), and 0.3 (c, f). For reference, corresponding isotropic plasticity predictions at $l = 50$ nm are included (a, c). A Voce-type isotropic hardening law relates the flow stress σ to the plastic strain ε^{p} as $\sigma = \sigma_0 + (\sigma_\infty - \sigma_0)[1 - \exp(-b\varepsilon^{\mathrm{p}})]$, with $\sigma_0 = 130$ MPa, $\sigma_\infty = 487.5$ MPa, and $b = 30$. Young's modulus and Poisson's ratio are set to $E = 76$ GPa and $\nu = 0.41$, respectively.

orientation effect on strain hardening may become more pronounced. However, with increasing compression, the likelihood of pore collapse and contact formation also grows, potentially dominating the overall mechanical response.

We note that the predicted mechanical response of NPG can be sensitive to the specific idealized microstructure due to the limited number of load-bearing ligaments, as highlighted in previous experimental and computational studies [32,80]. To assess the sensitivity to microstructural randomness, we conducted supplementary simulations using stochastic microstructures derived from recent FIB/SEM 3D reconstruction data [74]. The stochastic model features a ligament size of $l = 50$ nm and a solid fraction of $\varphi = 0.3$. The results demonstrate that the orientation-dependent trends in yield strength and strain hardening obtained from the periodic models are retained. Fig. 9 presents the corresponding stress–strain responses for the [001] and $[\bar{1}11]$ orientations, and Fig. 10 later shows that the same trends

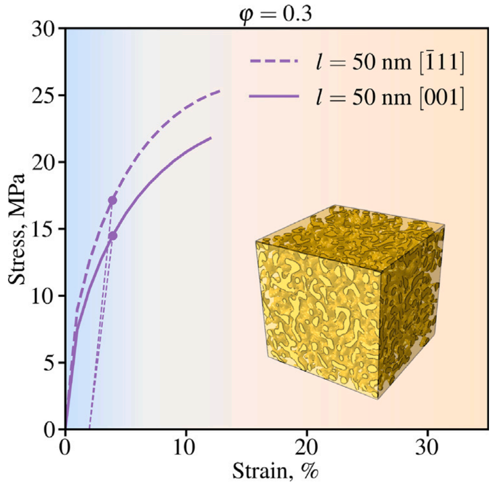

Fig. 9. Predicted stress–strain responses for the $[001]$ and $[\bar{1}11]$ crystal orientations, obtained from RVE simulations based on stochastic NPG microstructure models reconstructed from recent FIB/SEM 3D data [74]. The stochastic model corresponds to a ligament size of $l = 50$ nm and a solid fraction of $\varphi = 0.3$.

carry over to the scaling behavior of the normalized yield strength and hardening rate.

Fig. 10 summarizes the impact of crystallographic orientation on the normalized yield strength (a) and strain hardening rate (b) across different solid fractions. To improve the robustness of the scaling analysis, additional $[\bar{1}11]$ data points at $\varphi = 0.375$ are included, providing validation for a more reliable fit. The supplementary simulation results based on the reconstructed stochastic microstructure are also incorporated, with the corresponding data points falling below the diamond-network trends, likely due to reduced connectivity in the random ligament architecture. For the yield strength scaling in Fig. 10(a), a consistent trend emerges where NPG pillars oriented along $[\bar{1}11]$ exhibit systematically lower normalized yield strength compared to those aligned with $[001]$, regardless of ligament size. This difference arises from the distinct bulk yield strengths of the two orientations. For example, at $l = 50$ nm, the predicted yield strength is approximately 770 MPa for the $[\bar{1}11]$ orientation, compared to 460 MPa for the $[001]$ orientation. Because the $[\bar{1}11]$ orientation is intrinsically stronger in bulk single crystals, its normalized yield strength appears lower when referenced to its respective bulk value. Similar to the scaling trends observed previously, the fitted curves for different ligament sizes show an offset pattern, indicating that the size effect persists across orientations. A analogous trend is identified for the normalized strain hardening rate in Fig. 10(b). Smaller ligament sizes generally result in lower normalized hardening rates compared to their bulk counterparts. However, unlike the normalized yield strength, the normalized strain hardening behavior appears less sensitive to crystallographic orientation, indicating a more orientation-independent response across the ligament sizes and solid fractions studied.

Fig. 11(a–d) shows the probability density distributions of the local von Mises stresses, normalized by its mean value, for different ligament sizes, solid fractions, and crystallographic orientations at a fixed compression of $\varepsilon = 5$ %, shortly after yielding. In contrast, Fig. 11(e–f) presents the corresponding local bulk response. For comparison, predictions based on classical isotropic von Mises plasticity at $l = 50$ nm are also included in Fig. 11(a–d). This isotropic formulation, commonly applied to porous metals, neglects orientation-dependent effects. Here, the stress–strain response is calibrated to lie approximately between the two anisotropic, orientation-dependent cases ($[001]$ and $[\bar{1}11]$), see Fig. 8 (a, c). A subtle distinction arises between the $[001]$ and $[\bar{1}11]$ orientations. For $[\bar{1}11]$-oriented pillars, stress distributions exhibit higher peaks and broader tails, especially for the smallest ligaments ($l = 50$ nm) at high solid fractions ($\varphi = 0.3$), see Fig. 11(d). This suggests a wider range of stress states, indicating a more heterogeneous local stress distribution. Conversely, $[001]$-oriented pillars reveal lower peak stresses and a steeper decay at higher values, reflecting a more homogeneous stress distribution. Larger ligaments ($l = 402$ nm) exhibit more concentrated stress distributions, suggesting reduced local fluctuations and a shift toward bulk-like behavior. At $\varphi = 1.0$, see Fig. 11 (e-f), the stress distributions for the bulk reference are approximately half as wide as those at lower solid fractions, indicating

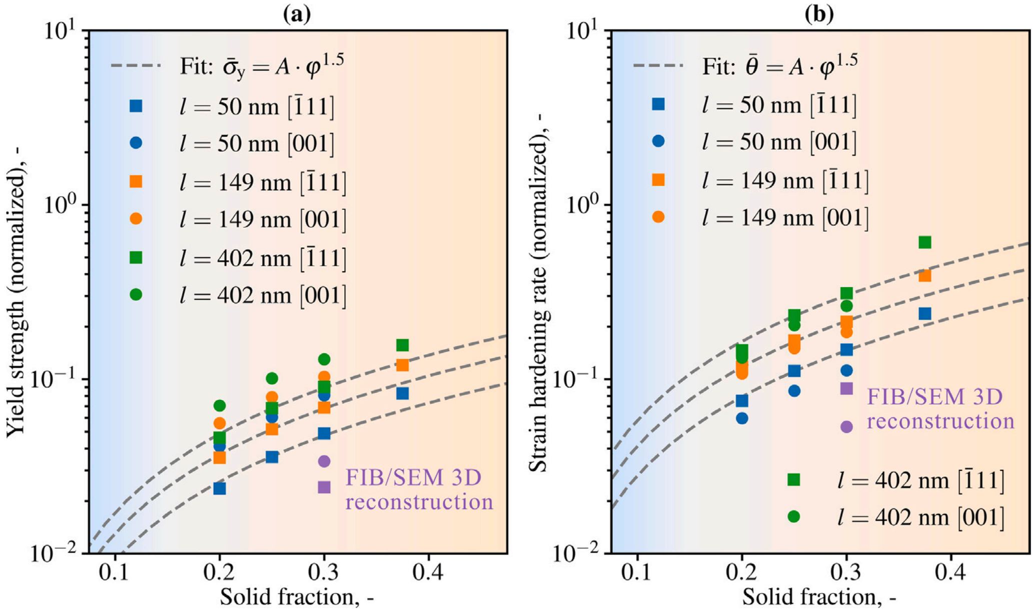

Fig. 10. Ligament size-dependent scaling of the predicted normalized yield strength (a) and strain hardening rate (b) for the initial $[001]$ and $[\bar{1}11]$ crystal orientations. Yield strength is determined at a 2 % strain offset and strain hardening rate at 5 % compressive strain, both normalized by the corresponding single crystal bulk values. Dashed lines indicate a modified Gibson–Ashby scaling fit to the numerical $[\bar{1}11]$ data. For validation of the scaling fit, an additional $[\bar{1}11]$ data set at a solid fraction of $\varphi = 0.375$ is included. To further examine the effect of microstructural randomness, supplementary results from simulations based on stochastic microstructures reconstructed from FIB/SEM 3D data [74] are also depicted.

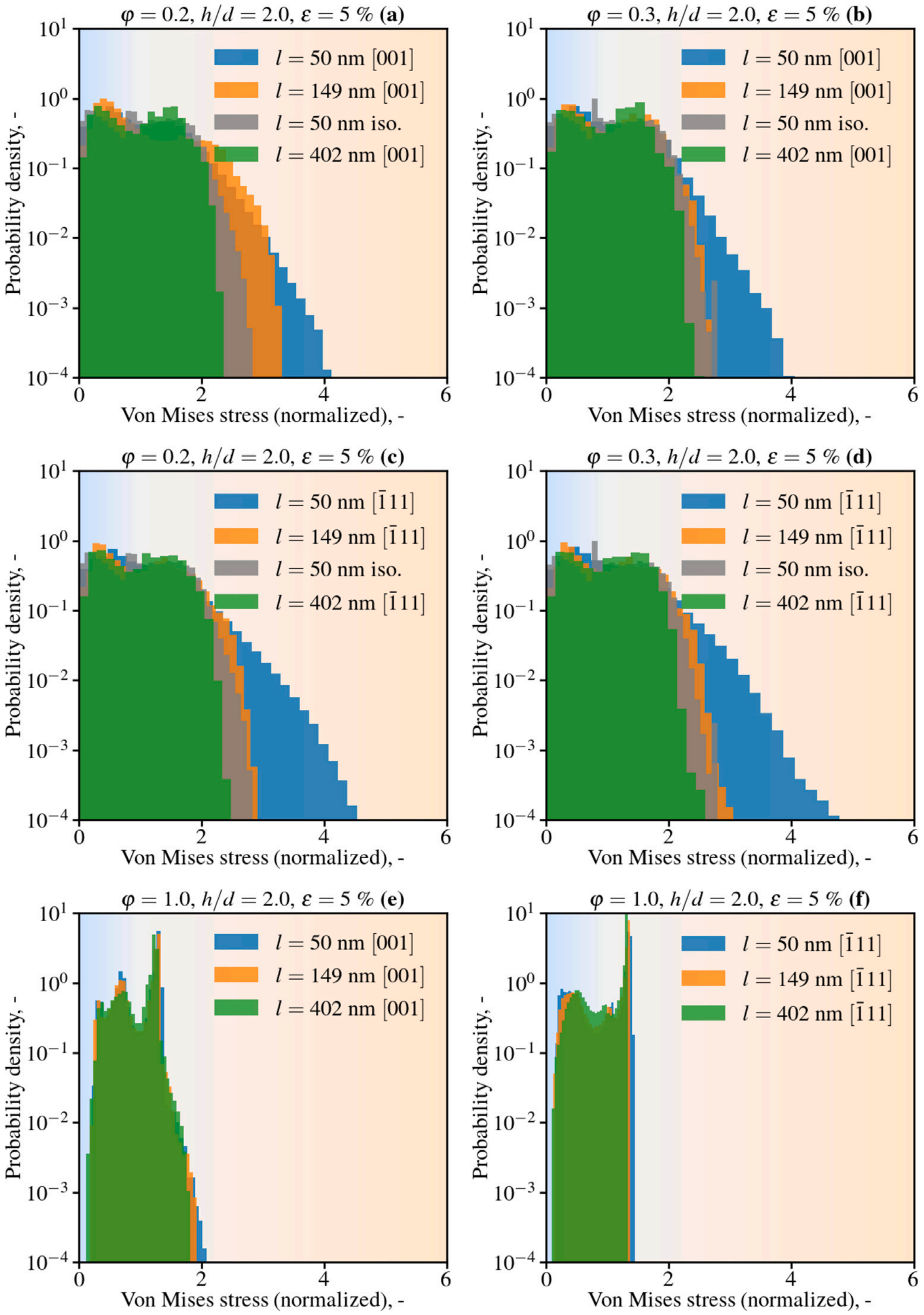

Fig. 11. Comparison of predicted local stress distributions for the initial [001] (a, b, e) and $[\bar{1}11]$ (c, d, f) crystal orientations. All distributions are acquired shortly after yielding at 5 % compression. The ligament sizes l are 50, 149, and 402 nm, with solid fractions φ of 0.2 (a, c), 0.3 (b, d), and 1.0 (e, f). For reference, corresponding isotropic plasticity predictions at $l = 50$ nm are included (a–d).

a more homogeneous stress state. These distributions primarily arise from inhomogeneities introduced by the micropillar geometry. For both [001] and $[\bar{1}11]$ orientations at $\varphi = 1.0$, the distributions peak sharply at lower stresses with minimal high-stress tails, contrasting with the broader, more heterogeneous stress distributions at lower solid fractions. For the case of isotropic plasticity predictions at a ligament size of $l = 50$ nm, the stress distribution is notably more homogeneous compared to orientation-dependent plasticity predictions. Interestingly, the isotropic predictions resemble more the anisotropic cases observed at larger ligament sizes, such as $l = 149$ nm. Consequently, although the stress–strain curves for isotropic and crystal plasticity are similar, the local stress distributions differ noticeably.

The corresponding stress contour plots and close-ups views in Fig. 12, shown at $\varepsilon = 5$ % compression strain for ligament sizes of $l = 50$ nm (a–h) and $l = 402$ nm (i–l), provide further insight into the local stress trends discussed above. As seen from these close-ups at $\varphi = 0.2$ and $\varphi = 0.3$, pillars with $[\bar{1}11]$ orientation exhibit more localized stress concentrations, aligning with the broader stress distributions. In

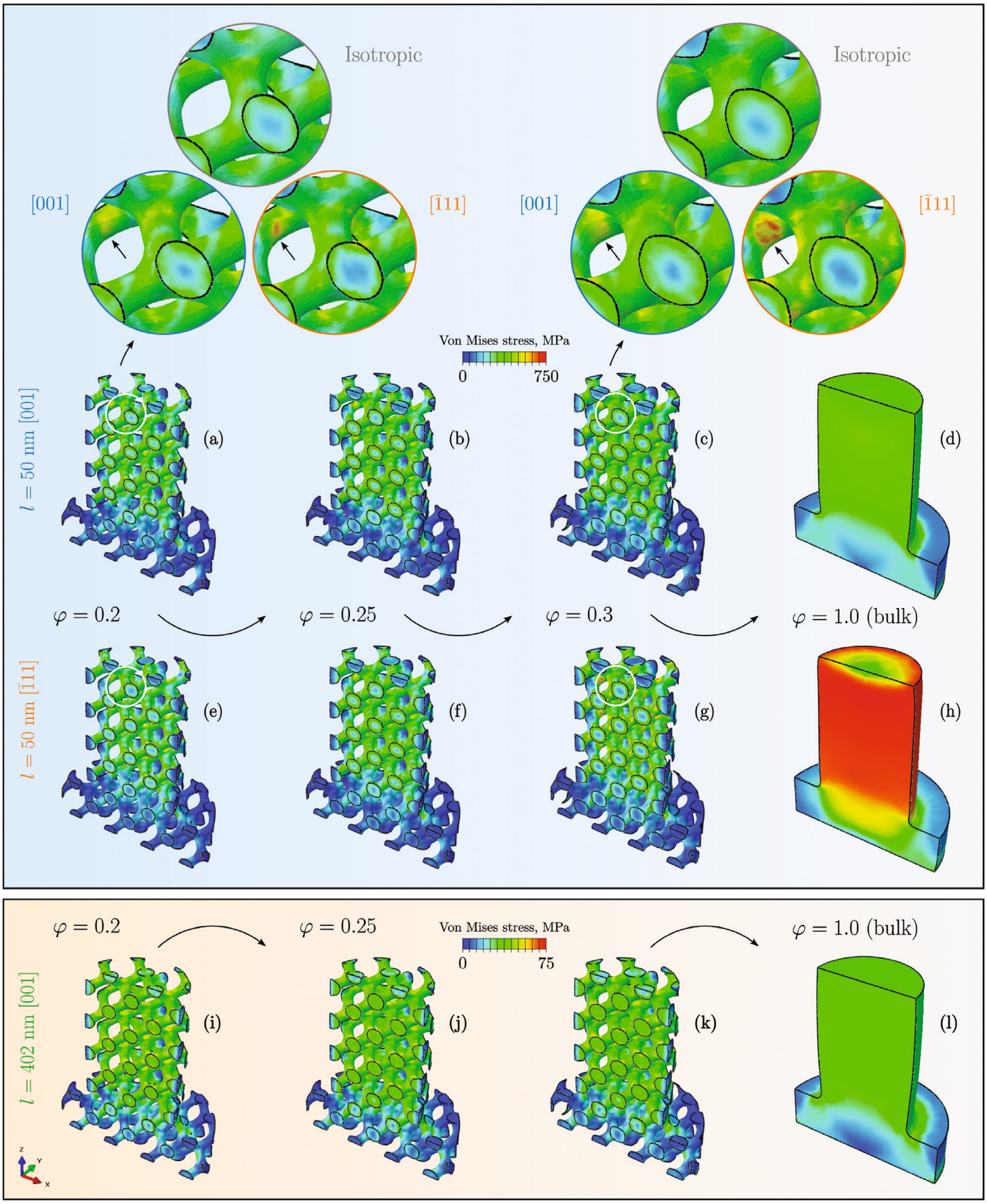

Fig. 12. Comparison of predicted von Mises stress contour plots for the initial [001] (a–d, i–l) and [$\bar{1}11$] (e–h) crystal orientations. All models are displayed in half-section at 5 % compression. The ligament sizes l are 50 nm (a–h) and 402 nm (i–l), with solid fractions φ of 0.2, 0.25, 0.3, and 1.0. Close-ups of individual ligaments highlight the differences in local stress concentration resulting from the [001] and [$\bar{1}11$] crystal orientation. For reference, corresponding close-ups based on isotropic plasticity are also included.

contrast, the [001]-oriented pillars exhibit a more uniform and narrower stress distribution. Overall, stress concentrations are predicted near ligament junctions. In the close-up views of the isotropic predictions, no distinct stress concentrations are observed, reflecting the narrower stress distributions. However, the stress distribution appears more similar to that of the [001] orientation. Additionally, the ligament size influences the local stress state, with larger ligaments (l = 402 nm) exhibiting more homogeneous stress fields, see Fig. 12(i–k).

5. Conclusions

In summary, an experimentally validated computational crystal plasticity approach is employed to systematically explore three key microstructural effects, including ligament size ($50 \le l \le 400$ nm), solid fraction ($0.2 \le \varphi \le 0.3$), and initial crystal orientation ([001] and [$\bar{1}11$]), on the single crystal NPG micropillar compression response, extending well beyond yielding. Key findings include:

- While the yield strength follows the expected 'smaller is stronger' trend, the strain hardening rate likewise increases with decreasing ligament size, and both exhibit power-law scaling with solid fraction.
- Crystal orientation analysis updates previous assumptions. While the onset of yielding remains orientation-independent, the harder $[\bar{1}11]$ orientation exhibits increased strain hardening, especially at higher solid fractions and smaller ligament sizes.
- Harder orientations, combined with higher solid fractions and smaller ligaments, lead to broader local stress distributions. Notably, NPG exhibits stress distributions nearly twice as wide as those in single crystal bulk material ($\varphi = 1.0$).
- Traditional isotropic plasticity predicts narrower, i.e. more homogeneous, local stress distributions in NPG compared to the crystal plasticity approach.

CRediT authorship contribution statement

Tim Fischer: Writing – original draft, Visualization, Validation, Software, Methodology, Investigation, Formal analysis, Conceptualization. **Norbert Huber:** Writing – review & editing, Supervision, Resources, Project administration, Funding acquisition.

Declaration of competing interest

The authors declare that they have no known competing financial interests or personal relationships that could have appeared to influence the work reported in this paper.

Acknowledgments

This work was supported by the Deutsche Forschungsgemeinschaft (DFG, German Research Foundation) through the Cluster of Excellence EXC 3120 BlueMat: Water-Driven Materials and the Hamburg Centre for Integrated Multiscale Materials Systems (CIMMS). The authors gratefully acknowledge S. Shi (Hamburg University of Technology) for insightful discussions and the TUHH Computing Center for providing access to the high-performance computing (HPC) cluster. Special thanks are extended to C.F.O. Dahlberg (KTH Royal Institute of Technology, Sweden) for providing the material subroutine used in Abaqus.

Data availability

Data will be made available on request.

References

[1] H.-J. Jin, J. Weissmüller, A material with electrically tunable strength and flow stress, Science 332 (6034) (2011) 1179–1182, http://dx.doi.org/10.1126/science.1202190.

[2] H.-J. Jin, J. Weissmüller, Bulk nanoporous metal for actuation, Adv. Eng. Mater. 12 (8) (2010) 714–723, http://dx.doi.org/10.1002/adem.200900329.

[3] J. Weissmüller, R.N. Viswanath, D. Kramer, P. Zimmer, R. Würschum, H. Gleiter, Charge-induced reversible strain in a metal, Science 300 (5617) (2003) 312–315, http://dx.doi.org/10.1126/science.1081024.

[4] J. Biener, A. Wittstock, L. Zepeda-Ruiz, M. Biener, V. Zielasek, D. Kramer, R. Viswanath, J. Weissmüller, M. Bäumer, A. Hamza, Surface-chemistry-driven actuation in nanoporous gold, Nat. Mater. 8 (2009) 47–51, http://dx.doi.org/10.1038/nmat2335.

[5] J. Weissmüller, R.C. Newman, H.-J. Jin, A.M. Hodge, J.W. Kysar, Nanoporous metals by alloy corrosion: Formation and mechanical properties, MRS Bull. 34 (8) (2009) 577–586, http://dx.doi.org/10.1557/mrs2009.157.

[6] H. Gleiter, J. Weissmüller, O. Wollersheim, R. Würschum, Nanocrystalline materials: a way to solids with tunable electronic structures and properties? Acta Mater. 49 (4) (2001) 737–745, http://dx.doi.org/10.1016/S1359-6454(00)00221-4.

[7] L.-Z. Liu, Y.-Y. Zhang, H. Xie, H.-J. Jin, Transition from homogeneous to localized deformation in nanoporous gold, Phys. Rev. Lett. 127 (2021) 095501, http://dx.doi.org/10.1103/PhysRevLett.127.095501.

[8] Y.-Y.Z. Ling-Zhi Liu, H.-J. Jin, On correlation between the hardness-to-strength ratio and the plastic Poisson's ratio of nanoporous gold, Mater. Res. Lett. 11 (6) (2023) 454–461, http://dx.doi.org/10.1080/21663831.2023.2181717.

[9] L.-Z.L. Peng Wu, H.-J. Jin, Monolayer oxide enhanced flow stress in nanoporous gold: the size dependence, Mater. Res. Lett. 6 (9) (2018) 508–514, http://dx.doi.org/10.1080/21663831.2018.1486337.

[10] J.R. Greer, J.T. De Hosson, Plasticity in small-sized metallic systems: Intrinsic versus extrinsic size effect, Prog. Mater. Sci. 56 (6) (2011) 654–724, http://dx.doi.org/10.1016/j.pmatsci.2011.01.005.

[11] L.-Z. Liu, X.-L. Ye, H.-J. Jin, Interpreting anomalous low-strength and low-stiffness of nanoporous gold: Quantification of network connectivity, Acta Mater. 118 (2016) 77–87, http://dx.doi.org/10.1016/j.actamat.2016.07.033.

[12] S. Shi, Y. Li, B.-N. Ngo-Dinh, J. Markmann, J. Weissmüller, Scaling behavior of stiffness and strength of hierarchical network nanomaterials, Science 371 (6533) (2021) 1026–1033, http://dx.doi.org/10.1126/science.abd9391.

[13] H.-J. Jin, L. Kurmanaeva, J. Schmauch, H. Rösner, Y. Ivanisenko, J. Weissmüller, Deforming nanoporous metal: Role of lattice coherency, Acta Mater. 57 (9) (2009) 2665–2672, http://dx.doi.org/10.1016/j.actamat.2009.02.017.

[14] X.-Y. Sun, G.-K. Xu, X. Li, X.-Q. Feng, H. Gao, Mechanical properties and scaling laws of nanoporous gold, J. Appl. Phys. 113 (2) (2013) 023505, http://dx.doi.org/10.1063/1.4774246.

[15] N. Mameka, K. Wang, J. Markmann, E.T. Lilleodden, J. Weissmüller, Nanoporous gold—Testing macro-scale samples to probe small-scale mechanical behavior, Mater. Res. Lett. 4 (1) (2016) 27–36, http://dx.doi.org/10.1080/21663831.2015.1094679.

[16] A. Hodge, J. Biener, J. Hayes, P. Bythrow, C. Volkert, A. Hamza, Scaling equation for yield strength of nanoporous open-cell foams, Acta Mater. 55 (4) (2007) 1343–1349, http://dx.doi.org/10.1016/j.actamat.2006.09.038.

[17] S. Bargmann, C. Soyarslan, E. Husser, N. Konchakova, Materials based design of structures: Computational modeling of the mechanical behavior of gold-polymer nanocomposites, Mech. Mater. 94 (2016) 53–65, http://dx.doi.org/10.1016/j.mechmat.2015.11.008.

[18] E. Husser, C. Soyarslan, S. Bargmann, Size affected dislocation activity in crystals: Advanced surface and grain boundary conditions, Extrem. Mech. Lett. 13 (2017) 36–41, http://dx.doi.org/10.1016/j.eml.2017.01.007.

[19] C. Dahlberg, Y. Saito, M. Öztop, J. Kysar, Geometrically necessary dislocation density measurements associated with different angles of indentations, Int. J. Plast. 54 (2014) 81–95, http://dx.doi.org/10.1016/j.ijplas.2013.08.008.

[20] H. Jeon, J. Markmann, S. Shi, Effects of structural hierarchy and size on mechanical behavior of nanoporous gold, Acta Mater. 273 (2024) 119954, http://dx.doi.org/10.1016/j.actamat.2024.119954.

[21] H. Jeon, J.-H. Woo, E. Song, J.-Y. Kim, Ligament size effect in creep of nanoporous gold, Int. J. Plast. 150 (2022) 103192, http://dx.doi.org/10.1016/j.ijplas.2021.103192.

[22] N.-R. Kang, E.-J. Gwak, H. Jeon, E. Song, J.-Y. Kim, Microstructural effect on time-dependent plasticity of nanoporous gold, Int. J. Plast. 109 (2018) 108–120, http://dx.doi.org/10.1016/j.ijplas.2018.05.011.

[23] J. Sanchez, L. Dammann, L. Gallardo, Z. Li, M. Fröba, R.H. Meißner, H.A. Stone, P. Huber, Deformation dynamics of nanopores upon water imbibition, PNAS 121 (38) (2024) e2318386121, http://dx.doi.org/10.1073/pnas.2318386121.

[24] B.-N.D. Ngô, A. Stukowski, N. Mameka, J. Markmann, K. Albe, J. Weissmüller, Anomalous compliance and early yielding of nanoporous gold, Acta Mater. 93 (2015) 144–155, http://dx.doi.org/10.1016/j.actamat.2015.04.021.

[25] J. Weissmüller, H.-L. Duan, D. Farkas, Deformation of solids with nanoscale pores by the action of capillary forces, Acta Mater. 58 (1) (2010) 1–13, http://dx.doi.org/10.1016/j.actamat.2009.08.008.

[26] E.-J. Gwak, H. Jeon, E. Song, N.-R. Kang, J.-Y. Kim, Twinned nanoporous gold with enhanced tensile strength, Acta Mater. 155 (2018) 253–261, http://dx.doi.org/10.1016/j.actamat.2018.06.009.

[27] D. Ma, P. Eisenlohr, E. Epler, C.A. Volkert, P. Shanthraj, M. Diehl, F. Roters, D. Raabe, Crystal plasticity study of monocrystalline stochastic honeycombs under in-plane compression, Acta Mater. 103 (2016) 796–808, http://dx.doi.org/10.1016/j.actamat.2015.11.016.

[28] D. Ma, P. Eisenlohr, P. Shanthraj, M. Diehl, F. Roters, D. Raabe, Analytical bounds of in-plane Young's modulus and full-field simulations of two-dimensional monocrystalline stochastic honeycomb structures, Comput. Mater. Sci. 109 (2015) 323–329, http://dx.doi.org/10.1016/j.commatsci.2015.07.041.

[29] H. Jeon, S. Lee, J.-Y. Kim, Tension-compression asymmetry in plasticity of nanoporous gold, Acta Mater. 199 (2020) 340–351, http://dx.doi.org/10.1016/j.actamat.2020.08.054.

[30] C.A. Volkert, E.T. Lilleodden, D. Kramer, J. Weissmüller, Approaching the theoretical strength in nanoporous au, Appl. Phys. Lett. 89 (6) (2006) 061920, http://dx.doi.org/10.1063/1.2240109.

[31] Y.-Y. Zhang, L. Zou, L.-Z. Liu, H. Xie, C.-H. Li, H.-J. Jin, Mechanical properties of unidirectional nanoporous gold under compression, Acta Mater. 235 (2022) 118078, http://dx.doi.org/10.1016/j.actamat.2022.118078.

[32] Y. Wu, J. Markmann, E.T. Lilleodden, On the consequences of intrinsic and extrinsic size effects on the mechanical response of nanoporous au, Mater. Des. 232 (2023) 112175, http://dx.doi.org/10.1016/j.matdes.2023.112175.

[33] D. Lee, X. Wei, M. Zhao, X. Chen, S.C. Jun, J. Hone, J.W. Kysar, Plastic deformation in nanoscale gold single crystals and open-celled nanoporous gold, Model. Simul. Mater. Sci. Eng. 15 (1) (2006) S181, http://dx.doi.org/10.1088/0965-0393/15/1/S15.

[34] D. Lee, X. Wei, X. Chen, M. Zhao, S. Jun, J. Hone, E.G. Herbert, W.C. Oliver, J.W. Kysar, Microfabrication and mechanical properties of nanoporous gold at the nanoscale, Scr. Mater. 56 (5) (2007) 437–440, http://dx.doi.org/10.1016/j.scriptamat.2006.08.069.

[35] S. Van Petegem, S. Brandstetter, R. Maass, A.M. Hodge, B.S. El-Dasher, J. Biener, B. Schmitt, C. Borca, H. Van Swygenhoven, On the microstructure of nanoporous gold: An X-ray diffraction study, Nano Lett. 9 (3) (2009) 1158–1163, http://dx.doi.org/10.1021/nl803799q.

[36] H. Guan, H. Xie, Z.-P. Luo, W.-K. Bao, Z.-S. You, Z. Jin, H.-J. Jin, Ultrastrong spinodoid alloys enabled by electrochemical dealloying and refilling, PNAS 120 (1) (2023) e2214773120, http://dx.doi.org/10.1073/pnas.2214773120.

[37] C.A. Volkert, E.T. Lilleodden, Size effects in the deformation of sub-micron au columns, Phil. Mag. 86 (33–35) (2006) 5567–5579, http://dx.doi.org/10.1080/14786430600567739.

[38] J.R. Greer, W.C. Oliver, W.D. Nix, Size dependence of mechanical properties of gold at the micron scale in the absence of strain gradients, Acta Mater. 53 (6) (2005) 1821–1830, http://dx.doi.org/10.1016/j.actamat.2004.12.031.

[39] G. Sparks, P.S. Phani, U. Hangen, R. Maaß, Spatiotemporal slip dynamics during deformation of gold micro-crystals, Acta Mater. 122 (2017) 109–119, http://dx.doi.org/10.1016/j.actamat.2016.09.026.

[40] J. Biener, A.M. Hodge, J.R. Hayes, C.A. Volkert, L.A. Zepeda-Ruiz, A.V. Hamza, F.F. Abraham, Size effects on the mechanical behavior of nanoporous au, Nano Lett. 6 (10) (2006) 2379–2382, http://dx.doi.org/10.1021/nl061978i.

[41] D. Raabe, D. Ma, F. Roters, Effects of initial orientation, sample geometry and friction on anisotropy and crystallographic orientation changes in single crystal microcompression deformation: A crystal plasticity finite element study, Acta Mater. 55 (13) (2007) 4567–4583, http://dx.doi.org/10.1016/j.actamat.2007.04.023.

[42] T. Loaiza, T. Fischer, R.P. Babu, P. Hedström, Micromechanical response of dual-hardening martensitic bearing steel before and after rolling contact fatigue, J. Mater. Res. Technol. 29 (2024) 4728–4734, http://dx.doi.org/10.1016/j.jmrt.2024.02.142.

[43] S. Breumier, S. Sao-Joao, A. Villani, M. Lévesque, G. Kermouche, High strain rate micro-compression for crystal plasticity constitutive law parameters identification, Mater. Des. 193 (2020) 108789, http://dx.doi.org/10.1016/j.matdes.2020.108789.

[44] S. Yan, H. Zhou, B. Xing, S. Zhang, L. Li, Q.H. Qin, Crystal plasticity in fusion zone of a hybrid laser welded al alloys joint: From nanoscale to macroscale, Mater. Des. 160 (2018) 313–324, http://dx.doi.org/10.1016/j.matdes.2018.09.031.

[45] L. Chen, T.E. James Edwards, F. Di Gioacchino, W.J. Clegg, F.P. Dunne, M.-S. Pham, Crystal plasticity analysis of deformation anisotropy of lamellar tial alloy: 3D microstructure-based modelling and in-situ micro-compression, Int. J. Plast. 119 (2019) 344–360, http://dx.doi.org/10.1016/j.ijplas.2019.04.012.

[46] S. Ha, S.H. Kayani, K. Lee, S. Park, J.G. Kim, J.B. Seol, H. Sung, Experimental and crystal plasticity finite element study of the deformation behavior of high-mn steel micropillars, Steel Res. Int. 94 (2) (2023) 2200254, http://dx.doi.org/10.1002/srin.202200254.

[47] J. Wang, C. Yang, P.D. Hodgson, Strain gradients in cu–fe thin films and multilayers during micropillar compression, Mater. Sci. Eng. A 651 (2016) 146–154, http://dx.doi.org/10.1016/j.msea.2015.10.105.

[48] D. Kupka, N. Huber, E. Lilleodden, A combined experimental-numerical approach for elasto-plastic fracture of individual grain boundaries, J. Mech. Phys. Solids 64 (2014) 455–467, http://dx.doi.org/10.1016/j.jmps.2013.12.004.

[49] D. Li, R. Li, K. Yuan, A. Chen, N. Guo, C. Xu, W. Zhang, In-plane combination of micropillars with distinct aspect ratios to resist overload-induced adhesion failure, Adv. Sci. 11 (28) (2024) 2400972, http://dx.doi.org/10.1002/advs.202400972.

[50] A. Cornec, E. Lilleodden, Numerical analysis of micropillar compression behaviour and stress-strain curve estimation verified on glass fused silica, Mater. Today Commun. 33 (2022) 104971, http://dx.doi.org/10.1016/j.mtcomm.2022.104971.

[51] A. Cornec, E. Lilleodden, Stress-strain curve estimation from micropillar compression with transverse contraction effect, Mater. Today Commun. 41 (2024) 110396, http://dx.doi.org/10.1016/j.mtcomm.2024.110396.

[52] H. Zhang, B. Schuster, Q. Wei, K. Ramesh, The design of accurate micro-compression experiments, Scr. Mater. 54 (2) (2006) 181–186, http://dx.doi.org/10.1016/j.scriptamat.2005.06.043.

[53] B. Roschning, N. Huber, Scaling laws of nanoporous gold under uniaxial compression: Effects of structural disorder on the solid fraction, elastic Poisson's ratio, Young's modulus and yield strength, J. Mech. Phys. Solids 92 (2016) 55–71, http://dx.doi.org/10.1016/j.jmps.2016.02.018.

[54] N. Huber, R. Viswanath, N. Mameka, J. Markmann, J. Weißmüller, Scaling laws of nanoporous metals under uniaxial compression, Acta Mater. 67 (2014) 252–265, http://dx.doi.org/10.1016/j.actamat.2013.12.003.

[55] J. Li, C. Tian, B. Lu, Y. Xian, R. Wu, G. Hu, R. Xia, Deformation behavior of nanoporous gold based composite in compression: A finite element analysis, Compos. Struct. 211 (2019) 229–235, http://dx.doi.org/10.1016/j.compstruct.2018.12.046.

[56] E. Griffiths, J. Wilmers, S. Bargmann, B.D. Reddy, Nanoporous metal based composites: Giving polymers strength and making metals move, J. Mech. Phys. Solids 137 (2020) 103848, http://dx.doi.org/10.1016/j.jmps.2019.103848.

[57] K. Hu, M. Ziehmer, K. Wang, E.T. Lilleodden, Nanoporous gold: 3D structural analyses of representative volumes and their implications on scaling relations of mechanical behaviour, Phil. Mag. 96 (32–34) (2016) 3322–3335, http://dx.doi.org/10.1080/14786435.2016.1222087.

[58] L. Lührs, B. Zandersons, N. Huber, J. Weissmüller, Plastic Poisson's ratio of nanoporous metals: A macroscopic signature of tension–compression asymmetry at the nanoscale, Nano Lett. 17 (10) (2017) 6258–6266, http://dx.doi.org/10.1021/acs.nanolett.7b02950.

[59] J. Jiao, N. Huber, Deformation mechanisms in nanoporous metals: Effect of ligament shape and disorder, Comput. Mater. Sci. 127 (2017) 194–203, http://dx.doi.org/10.1016/j.commatsci.2016.10.035.

[60] C. Soyarslan, S. Bargmann, M. Pradas, J. Weissmüller, 3D stochastic bicontinuous microstructures: Generation, topology and elasticity, Acta Mater. 149 (2018) 326–340, http://dx.doi.org/10.1016/j.actamat.2018.01.005.

[61] H.-H. Cho, Y.-C.K. Chen-Wiegart, D.C. Dunand, Finite element analysis of mechanical stability of coarsened nanoporous gold, Scr. Mater. 115 (2016) 96–99, http://dx.doi.org/10.1016/j.scriptamat.2016.01.011.

[62] J. Erlebacher, M.J. Aziz, A. Karma, N. Dimitrov, K. Sieradzki, Evolution of nanoporosity in dealloying, Nature 410 (6827) (2001) 450–453, http://dx.doi.org/10.1038/35068529.

[63] T. Fischer, N. Huber, Designing microcompression experiments for nanoporous metals via computational plasticity, Mater. Des. 258 (2025) 114550, http://dx.doi.org/10.1016/j.matdes.2025.114550.

[64] Y. Huang, A user-material subroutine incorporating single crystal plasticity in the ABAQUS finite element program, Harv. Univ. Rep. Mech. 178 (1991).

[65] E. Schmid, W. Boas, Kristallplastizität – Mit Besonderer Berücksichtigung der Metalle, vol. 17, Springer-Verlag, Berlin Heidelberg, 1935.

[66] J. Hutchinson, Bounds and self-consistent estimates for creep of polycrystalline materials, Proc. R. Soc. A: Math. Phys. Eng. Sci. 348 (1652) (1976) 101–127.

[67] D. Peirce, R. Asaro, A. Needleman, Material rate dependence and localized deformation in crystalline solids, Acta Metall. 31 (12) (1983) 1951–1976, http://dx.doi.org/10.1016/0001-6160(83)90014-7.

[68] S.R. Kalidindi, Incorporation of deformation twinning in crystal plasticity models, J. Mech. Phys. Solids 46 (2) (1998) 267–290, http://dx.doi.org/10.1016/S0022-5096(97)00051-3.

[69] E.O. Hall, The deformation and ageing of mild steel: III discussion of results, Proc. Phys. Soc. Lond. Sect. B 64 (9) (1951) 747, http://dx.doi.org/10.1088/0370-1301/64/9/303.

[70] N. Petch, The cleavage strength of polycrystals, J. Iron. Steel Res. Int. 174 (1953) 25–28.

[71] S. Mathesan, D. Mordehai, On the yielding and densification of nanoporous au nanopillars in molecular dynamics simulations, Comput. Mater. Sci. 191 (2021) 110307, http://dx.doi.org/10.1016/j.commatsci.2021.110307.

[72] I. Kovács, G. Vörös, On the mathematical description of the tensile stress-strain curves of polycrystalline face centered cubic metals, Int. J. Plast. 12 (1) (1996) 35–43, http://dx.doi.org/10.1016/S0749-6419(95)00043-7.

[73] T. Przybilla, Z. Xie, A. Prakash, E. Thiess, F. Niekiel, B.A. Zubiri, M. Mačković, P. Schweizer, J. Guénolé, S.T. Kelly, H.A. Bale, D. Wang, S. Sandfeld, E. Bitzek, E. Spiecker, Revealing nanoscale plasticity of metallic nanosponges with correlative and scale-bridging 3D microscopy and modelling, Commun. Mater. 6 (1) (2025) 204, http://dx.doi.org/10.1038/s43246-025-00914-z.

[74] Y. Li, K. Hu, E.T. Lilleodden, N. Huber, Datasets for structural and mechanical properties of nanoporous networks from FIB reconstruction, Data Brief 63 (2025) 112152, http://dx.doi.org/10.1016/j.dib.2025.112152.

[75] R. Maaß, S. Van Petegem, D. Ma, J. Zimmermann, D. Grolimund, F. Roters, H. Van Swygenhoven, D. Raabe, Smaller is stronger: The effect of strain hardening, Acta Mater. 57 (20) (2009) 5996–6005, http://dx.doi.org/10.1016/j.actamat.2009.08.024.

[76] M.D. Uchic, D.M. Dimiduk, J.N. Florando, W.D. Nix, Sample dimensions influence strength and crystal plasticity, Science 305 (5686) (2004) 986–989, http://dx.doi.org/10.1126/science.1098993.

[77] N. Huber, A strategy for dimensionality reduction and data analysis applied to microstructure–property relationships of nanoporous metals, Materials 14 (8) (2021).

[78] B. Engelman, S. Mathesan, T. Fedyaeva, A. Bisht, E. Rabkin, D. Mordehai, Deformation behavior of nanoporous gold nanoparticles during compression, Acta Mater. 286 (2025) 120723, http://dx.doi.org/10.1016/j.actamat.2025.120723.

[79] L.J. Gibson, M.F. Ashby, Cellular solids: Structure and properties, second ed., in: Cambridge Solid State Science Series, Cambridge University Press, 1997.

[80] S. Mathesan, D. Mordehai, Size-dependent elastic modulus of nanoporous au nanopillars, Acta Mater. 185 (2020) 441–452, http://dx.doi.org/10.1016/j.actamat.2019.12.018.